THE ASTROPHYSICAL JOURNAL, 504:344–358, 1998 September 1

WFPC2 STUDIES OF THE CRAB NEBULA. II. IONIZATION STRUCTURE OF THE CRAB FILAMENTS[1]

RAVI SANKRIT,[2] J. JEFF HESTER,[2] P. A. SCOWEN,[2] GILDA E. BALLESTER,[3] CHRISTOPHER J. BURROWS,[4] JOHN T. CLARKE,[3] DAVID CRISP,[5] R. W. EVANS,[5] JOHN S. GALLAGHER III,[6] RICHARD E. GRIFFITHS,[7] JOHN G. HOESSEL,[6] JON A. HOLTZMAN,[8] JOHN KRIST,[4] JEREMY R. MOULD,[9] KARL R. STAPELFELDT,[5] JOHN T. TRAUGER,[5] ALAN WATSON,[10] AND JAMES A. WESTPHAL[11]

Received 1998 January 21; accepted 1998 April 3

ABSTRACT

Narrowband images of the Crab Nebula taken with the *Hubble Space Telescope* (*HST*) WFPC2 show the morphology and ionization structure of the filaments in great detail. At *HST* resolution, low- and high-ionization emission from filaments in the Crab differ in two complementary respects. First, low-ionization emission is found to be concentrated in very sharp structures, while high-ionization emission is predominantly found in a much more diffuse component. For example, approximately 80% of emission from [O I] λ6300 arises in features with scales of less than 0.″5, while only 10% of [O III] λ5007 emission arises in such compact structures. Second, individual filaments are found to lie along a sequence of ionization structures, ranging from features in which all lines are concentrated in the same compact volume through features with low-ionization cores surrounded by high-ionization envelopes. Hester and coworkers proposed in 1996 that this sequence can be understood as the result of the nonlinear development of magnetic Rayleigh-Taylor (R-T) instabilities along the interface between the Crab synchrotron nebula and swept-up ejecta.

We present photoionization models of cylindrically symmetrical filaments consisting of a quadratic core surrounded by an extended envelope. A good deal of the observed variation in filament structure in the Crab can be matched by varying the assumed density profiles in these models. This implies that variations in the development of R-T instabilities in the Crab account for much of the spectral variation within the remnant. We also present a photoionization model of a uniform, low-density medium, which reasonably matches the extended diffuse component that dominates the high-ionization emission. This envelope model produces strong [O III] but virtually no [O I]. While the He I/Hβ ratio remains fairly constant throughout a range of filament models, this ratio is a factor of 5 lower in the envelope model. We find that the apertures used in ground-based spectroscopy of the Crab generally include emission from several discrete filaments as well as a component of diffuse emission. This places a fundamental limit on what can be inferred reliably from comparison of spectra with one-dimensional photoionization models. Many filament cores coincide with dust extinction features seen in a continuum image of the Crab. We consider one such feature in detail and find that the extinction of about 1.2 mag suggests that the dust-to-gas mass ratio may be an order of magnitude higher than is typical in the interstellar medium.

Subject headings: ISM: individual (Crab Nebula) — ISM: structure — supernova remnants

1. INTRODUCTION

The Crab Nebula is the remnant of the Supernova explosion of A.D. 1054. It lies about 200 pc away from the Galactic plane in a region of low density. There is no evidence of interaction of the ejecta with ambient material. This means that the filaments (which consist of ejected material) are most likely uncontaminated by interstellar or circumstellar material. This gives us the opportunity of understanding the material processing that took place in the presupernova star and during the supernova explosion by studying the composition of the filaments. The filaments form a cagelike structure around the outer edges of the amorphous Crab synchrotron nebula. The synchrotron nebula is a region of magnetized plasma powered by the spin-down luminosity of the central pulsar. Synchrotron radiation from the nebula photoionizes the filaments, which emit a rich spectrum of line radiation.

Many studies have been done in which filament spectra have been analyzed to understand the composition of filaments. Lacking high spatial resolution, the observations have never isolated the spectrum of an individual filament, and this has been an inherent limitation of all these studies. (An excellent account of the study of Crab filament spectra is given in § 3 of Davidson & Fesen 1985, hereafter DF.) For example, the sophisticated photoionization models of Henry & MacAlpine (1982, hereafter HM) and Péquignot & Dennefeld (1983, hereafter PD) were successful in showing that power-law photoionization can indeed explain the spectra of the Crab filaments, but the observations they had to constrain their models were the average spectra of regions including more than a single filament as well as

[1] Based on observations with the NASA/ESA *Hubble Space Telescope*, obtained at the Space Telescope Science Institute, which is operated by AURA, Inc., under NASA contract 5-26555.

[2] Department of Physics and Astronomy, Box 871504, Arizona State University, Tempe, AZ 85287-1504.
[3] University of Michigan, Ann Arbor, MI 48109.
[4] Space Telescope Science Institute, Baltimore, MD 21218.
[5] Jet Propulsion Laboratory, Pasadena, CA 91109.
[6] University of Wisconsin-Madison, Madison, WI 53706.
[7] Carnegie Mellon University, Pittsburgh, PA 15213.
[8] New Mexico State University, Las Cruces, NM 88003.
[9] Mount Stromlo and Siding Springs Observatories, Australian National University, Weston Creek Post Office, ACT 2611, Australia.
[10] Instituto de Astronomia-UNAM, Morelia, Michoacan, Mexico.
[11] California Institute of Technology, Pasadena, CA 91125.

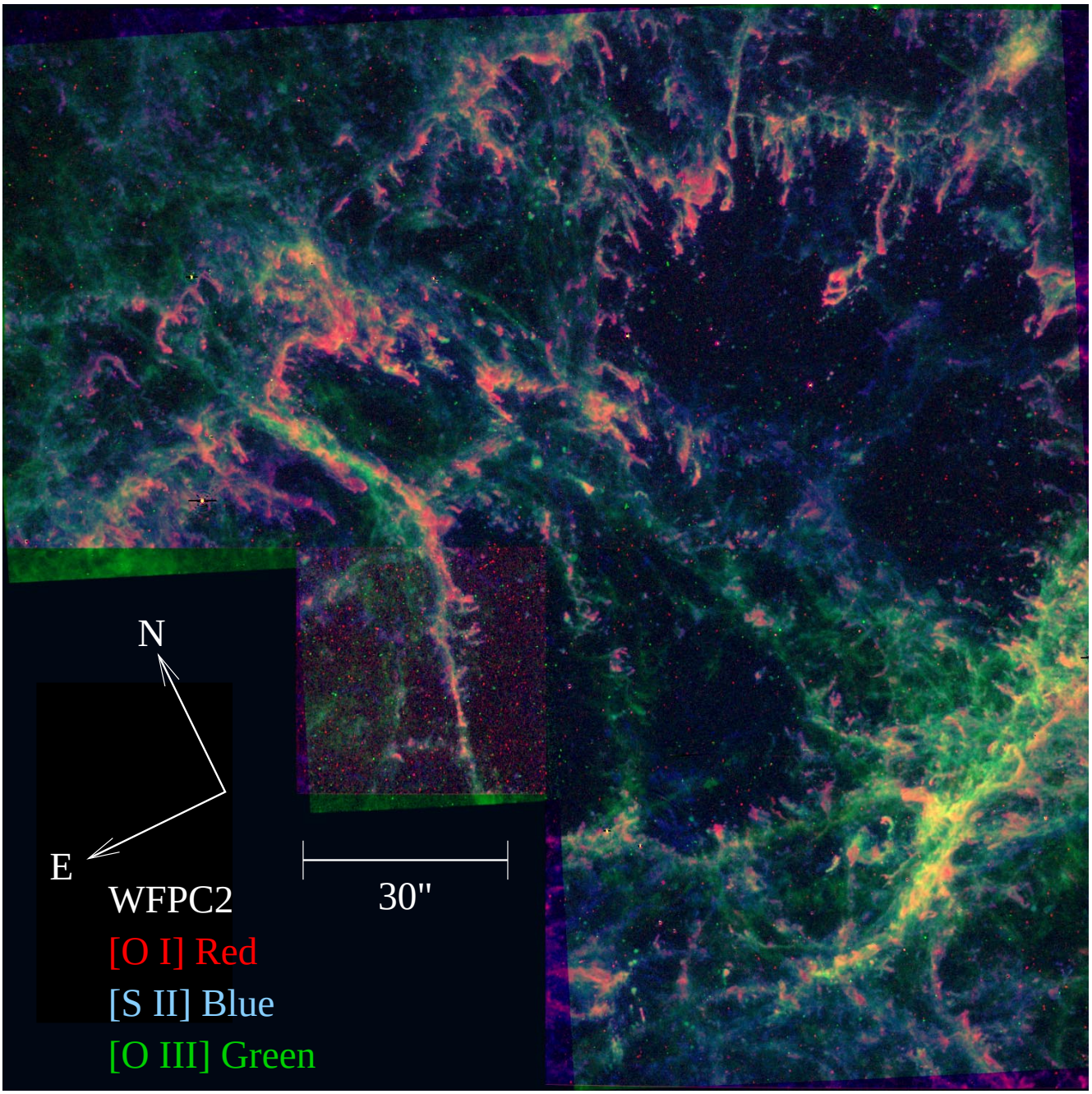

FIG. 1.—Three-color image of the Crab Filaments showing the full field of view of the *HST* observations. [O I] λ6300 is shown in red, [S II] $\lambda\lambda$6716, 6731 is shown in blue, and [O III] λ5007 is shown in green.

diffuse emission between filaments. Davidson (1987) used a spatial scanning technique to observe a spectrum integrated over the whole Crab. He pointed out that the overall nebular spectrum closely resembled a composite spectrum of a few particular filaments. More recently, the long-slit spectra and line filter images presented by MacAlpine et al. (1989) and the line filter images of Hester et al. (1990) emphasized the importance that the morphology of the filaments had on their emission. In particular, Hester et al. (1990) pointed out the necessity of considering the ionization stratification of individual filaments in interpreting their spectra.

A significant advance in the study of Crab filaments has been made recently, with narrowband *Hubble Space Telescope* (*HST*) images of the Crab resolving structures at the subarcsecond scale (Hester et al. 1996, hereafter H96; Blair et al. 1997). These images allow us to study the morphology and ionization structure of individual filaments in great detail. One immediate issue that arises from these data is the question of what is meant by the term "filament." Traditionally, the term "filament" has been used to refer to the macroscopic structures seen in ground-based images of the Crab. Hence one might speak of a filament running from one side of the Crab to the other. However, at *HST* resolution these structures break up into many smaller concentrations of emission. It is these smaller structures that constitute physically discrete units within the nebula, and it is to these structures that we apply the term "filament."

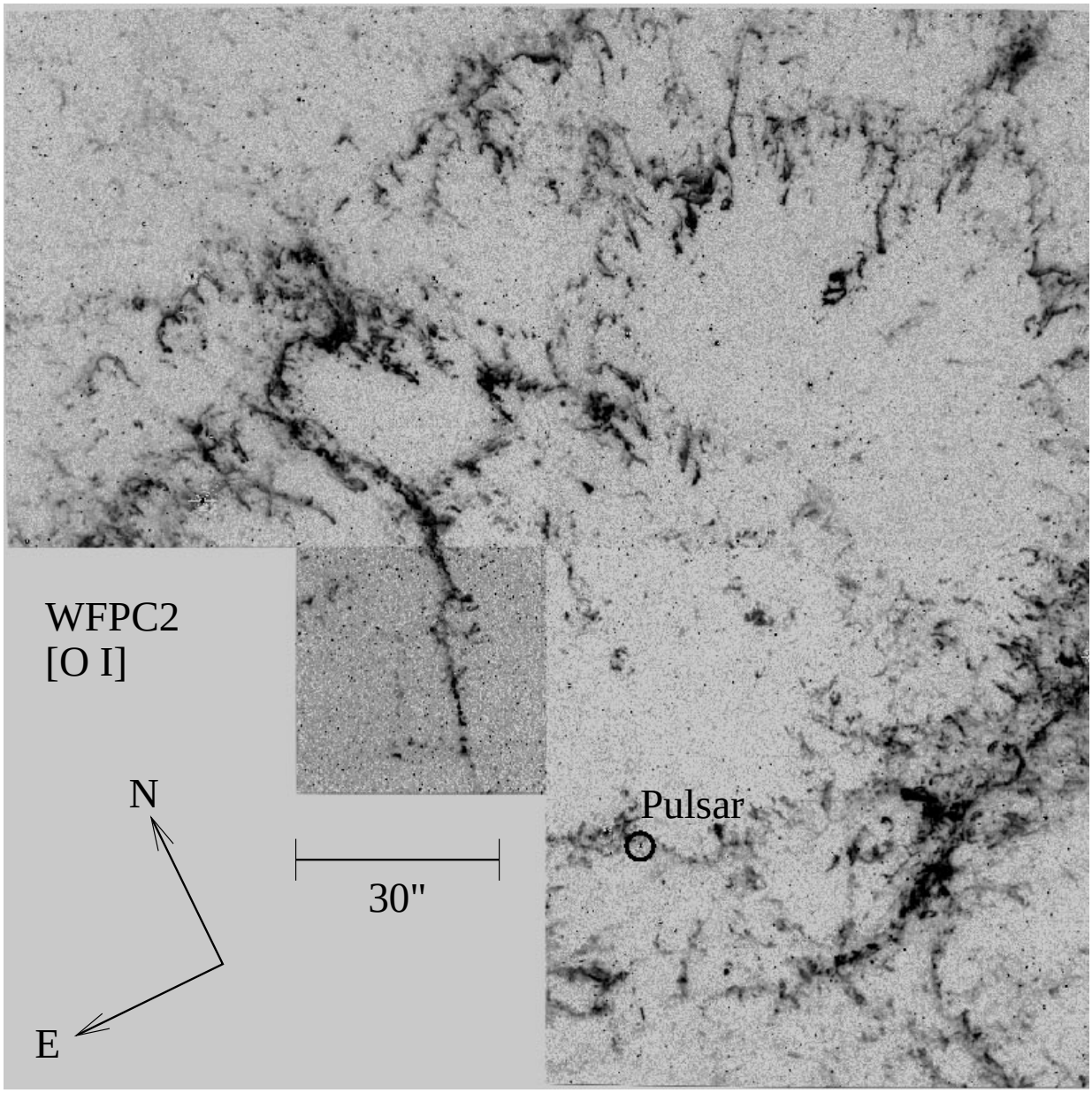

FIG. 2.—F631N filter image, which isolates the [O I] λ6300 emission. The structures are sharp, with the brightest parts tracing out the dense regions. The position of the Crab Pulsar is circled, a quarter of the way up and a little to the right of center.

H96 argue on the basis of the *HST* images that the filaments in the Crab are the result of Rayleigh-Taylor (R-T) instabilities between the synchrotron nebula and the denser ejecta on which it is pushing. While this idea is not new (e.g., DF), by comparing the filament morphologies with magnetohydrodynamic calculations (Jun, Norman, & Stone 1995), H96 provide a quantitative connection between filament structure and our theoretical understanding of the growth of magnetic R-T instabilities. Specifically, H96 found that the structure of Crab filaments generally lies along a sequence resulting from variations in the importance of the magnetic field during the nonlinear development of the instability. A significant aspect of this picture is the observed presence of a thin "skin" of high-ionization emission that traces the interface between the synchrotron nebula and the ejecta and connects the tops of the R-T fingers that protrude radially into the nebula. A consideration of the properties of the skin tracing the R-T unstable interface shows that it is most likely to be the cooling region behind a shock that is driven by the pressure of the synchrotron nebula into an extended remnant of freely expanding ejecta (Sankrit & Hester 1997). This picture has been confirmed recently by the calculations of Jun (1998).

One aspect of the progression in filament structure discussed by H96 is a sequence of ionization structures ranging from filaments in which all lines emerge from the same tightly confined volume to filaments that show pronounced stratification with high-ionization emission surrounding low-ionization emission. In the present paper we turn our attention to a better understanding of the ionization structure and overall spectrum emitted by filaments. In § 2 we summarize the *HST*-WFPC2 observations. In § 3 we discuss the structure of the Crab filaments seen in these images, emphasizing the differences in structure seen in

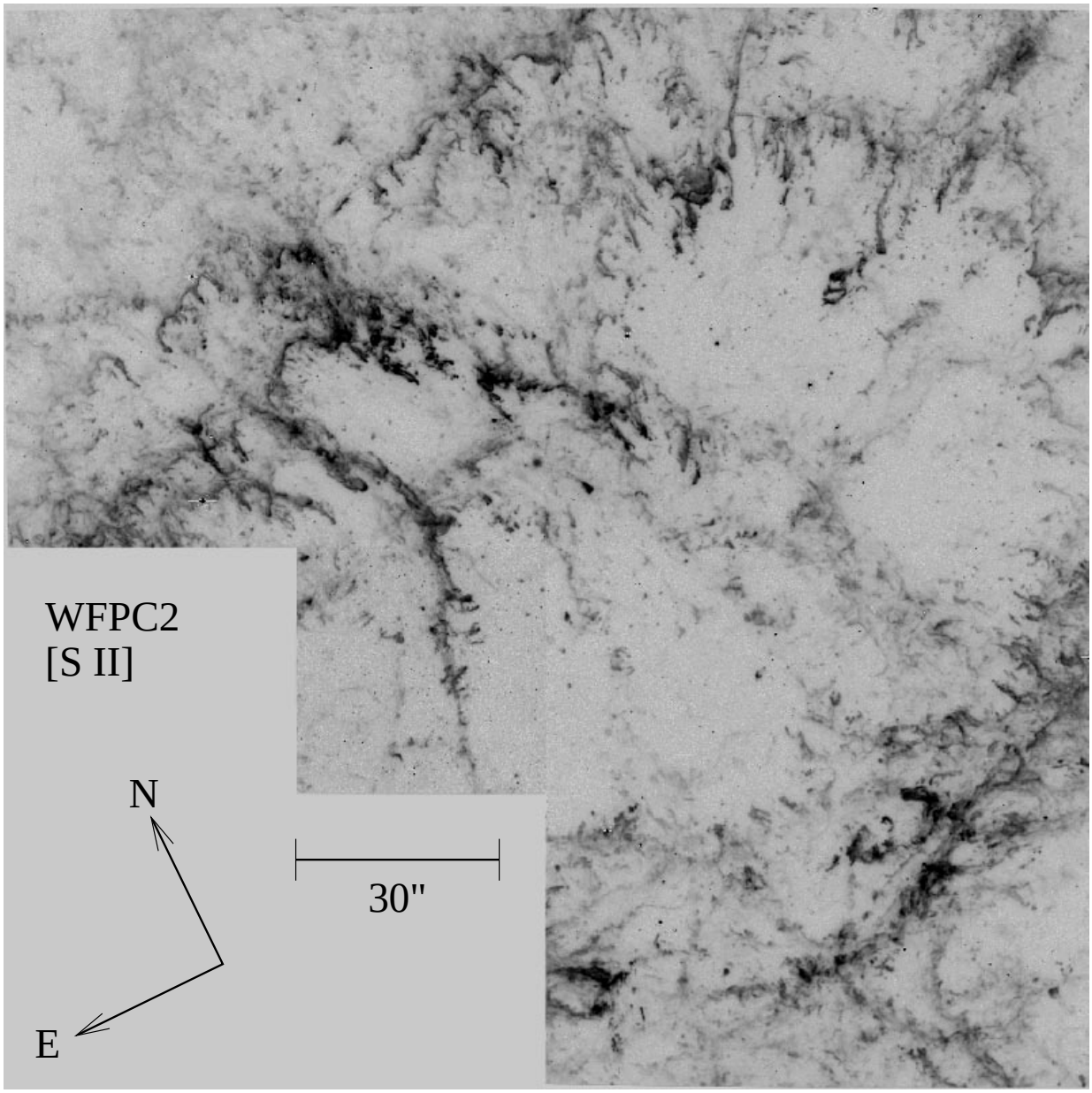

FIG. 3.—F673N filter image, which isolates the [S II] λλ6716, 6731 emission. The [S II] traces out the same features as [O I]; however, in a number of regions the [S II] is somewhat more diffuse.

emission from high- and low-ionization species. In § 4 we present cylindrically symmetrical photoionization models for individual filaments that are representative of the sequence of filament structures discussed by H96. In § 5 we discuss some implications of our study. In § 6 we present and discuss an example of the occurrence of dust in a dense filament core, and § 7 is a summary of our results.

2. OBSERVATIONS

Images of a field in the northern part of the Crab Nebula were obtained with the WFPC2 camera on board the *HST* in 1994 February. Two 2000 s exposures were taken through each of seven line filters—F375N ([O II] λ3727), F469N (He II λ4686), F487N (Hβ λ4861), F502N ([O III] λ5007), F588N (He I λ5876), F631N ([O I] λ6300), and F673N ([S II] λλ6716, 6731). In addition, two 1000 s exposures were taken through the line-free F547M continuum filter. The images were processed using locally developed Interactive Data Language routines. Individual frames taken through each filter were compared to remove cosmic rays, and the F547M image was used to subtract the synchrotron nebula continuum from the line filter images. The line intensities from filaments were obtained using the prescription given in Holtzman et al. (1995) and dereddened using $E_{B-V} = 0.47$ (DF and references therein).

In Figure 1 we show a three-color rendition of the entire WFPC2 field of view. The images on the individual cameras have been mosaicked. The [O I] image is displayed in red, the [S II] image is displayed in blue, and the [O III] image is displayed in green. At the distance of the Crab Nebula (taken to be 2000 pc), the scale of the images is approximately 3×10^{16} cm arcsec^{-1}. The long side of the irregular field of view of the WFPC2 corresponds to about 1.6 pc. In Figures 2–4 the mosaicked images through the [O I], [S II],

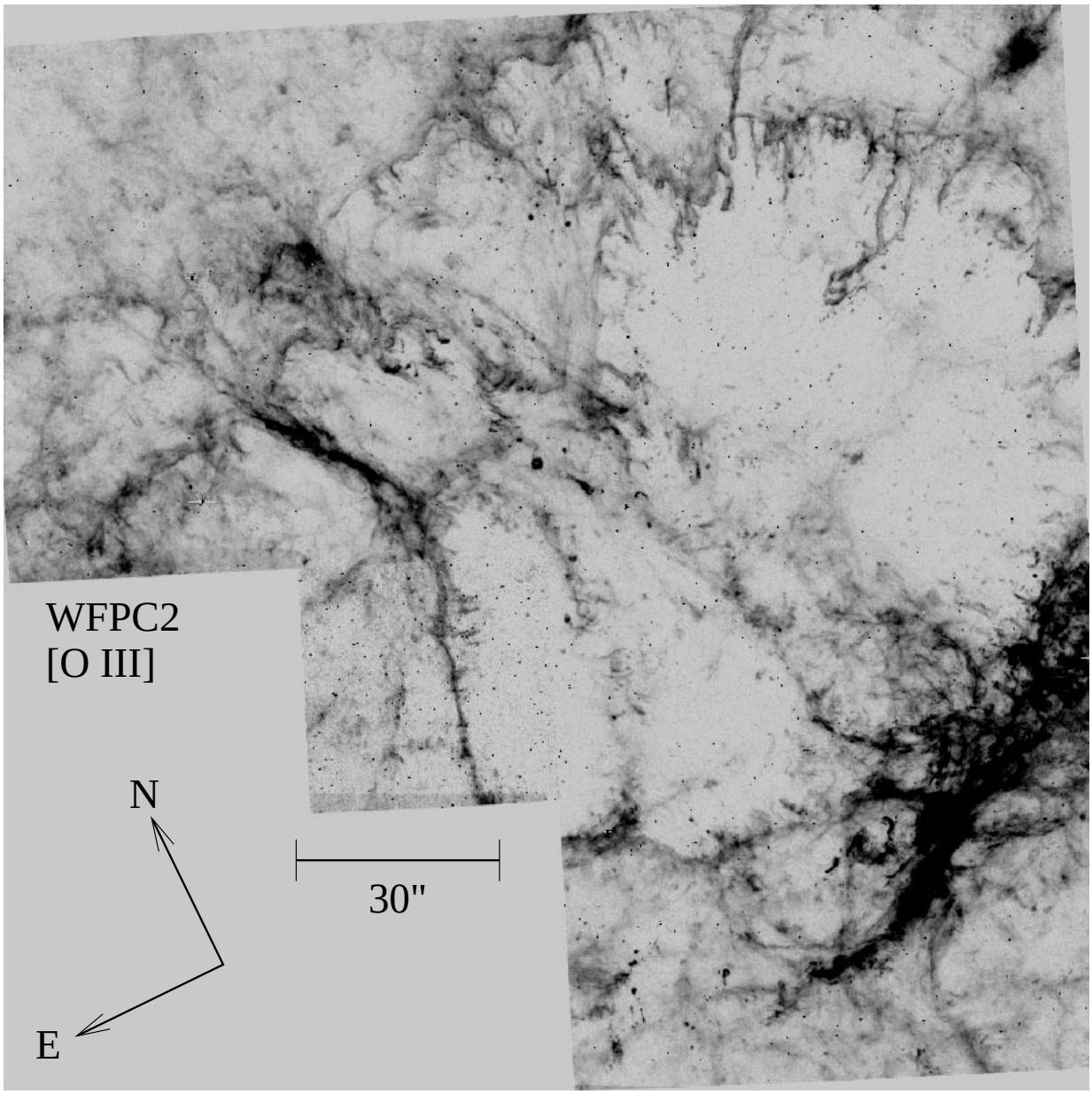

FIG. 4.—F502N filter image, which isolates the [O III] λ5007 emission. The morphology of the filaments in this high-ionization line is significantly different than in the low-ionization lines shown in Figs. 2 and 3. There is [O III] emission from regions around the bright [O I] regions and also more diffuse emission that has no counterpart in the [O I] image.

and [O III] filters are shown individually. Figure 5 shows both the He I and the He II images. The position of the pulsar, about one fourth of the way up near the center line, is indicated by a circle on the F631N image.

3. THE STRUCTURE OF THE CRAB FILAMENTS

The appearance of the Crab filaments seen in the emission from low-ionization potential species is very different from their appearance in the emission from high–ionization potential species. Generally speaking, the low-ionization emission tends to come from very compact regions, while the high-ionization emission is more extended. On larger scales this difference was noted in ground-based images by Chevalier & Gull (1975), who found that the low-ionization emission comes from a region within a high-ionization region prominent in [O III]. Blair et al. (1997) also note the diffuse high-ionization gas in the Crab filaments.

This difference between low- and high-ionization gas is apparent when comparing the [O I] and [S II] images on the one hand (Figs. 2 and 3) with the [O III] image on the other. The [O I] emission comes almost entirely from bright, dense knots with typical sizes less than 1.″0 and from structures which, even if they are fairly extended along one dimension, have widths less than 1.″0. The [S II] emission also arises mainly from these narrow, compact features, but a careful examination of Figure 1 or comparison between Figures 2 and 3 shows there are a number of regions where the [S II] is somewhat more diffuse than the [O I]. The [O III] emission, in contrast to the [O I] and [S II] emission, comes from much more extended regions of diffuse gas.

In order to quantify this observed difference, we generated high-pass filtered [O I], [S II], and [O III] images and used these to distinguish between regions of compact emission and regions of more diffuse emission. Gaussian-filtered

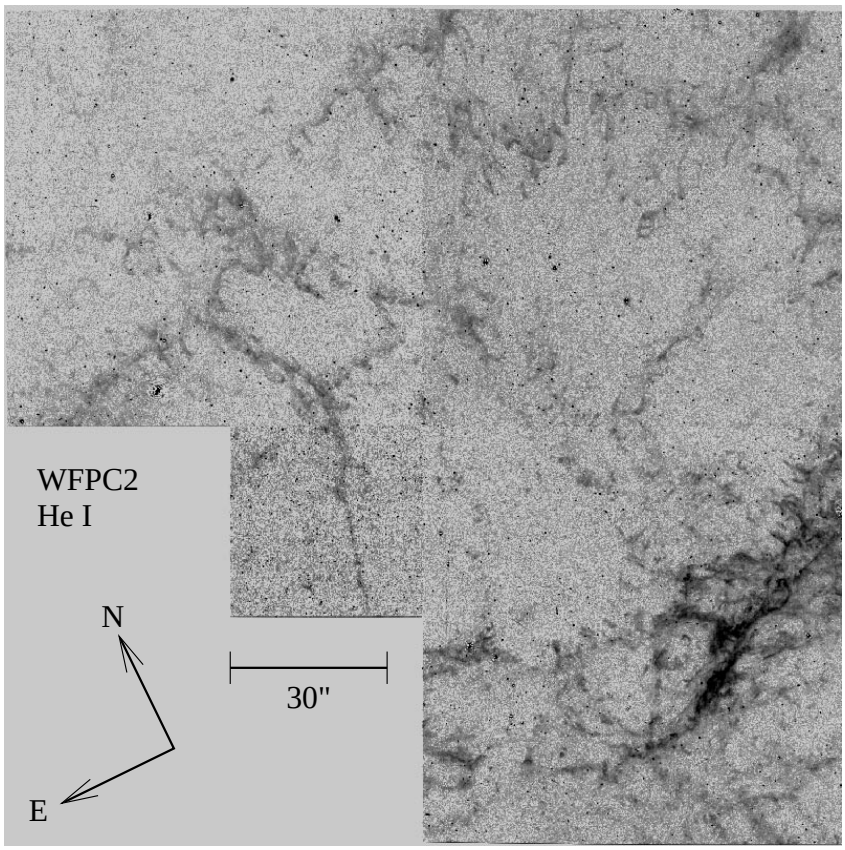

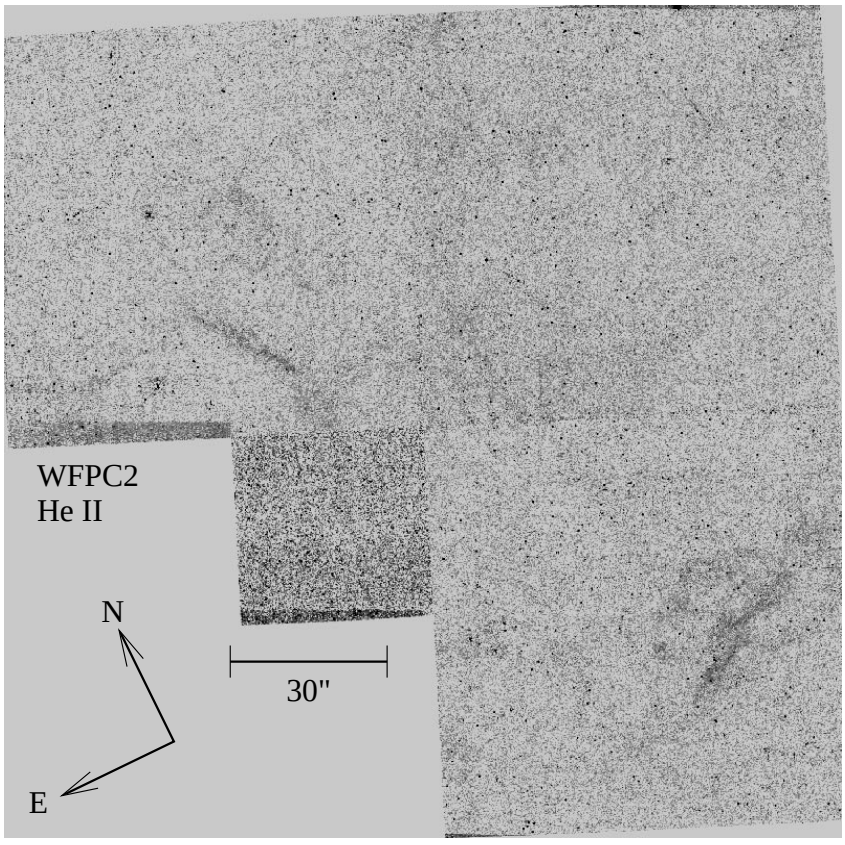

FIG. 5.—*Top:* F588N filter image, which isolates the He I λ5876 emission. Although the signal is low, the main filamentary features seen in the [O I] and [S II] images are seen. The contrast between the "high-helium band" in the lower right of the image and the rest of the filaments is very clear. *Bottom:* F469N filter image, which isolates the He II λ4686 emission. The signal is very low, and the only features seen are parts of the "high-helium band" and the "northern hook" to the left, just above the planetary camera field.

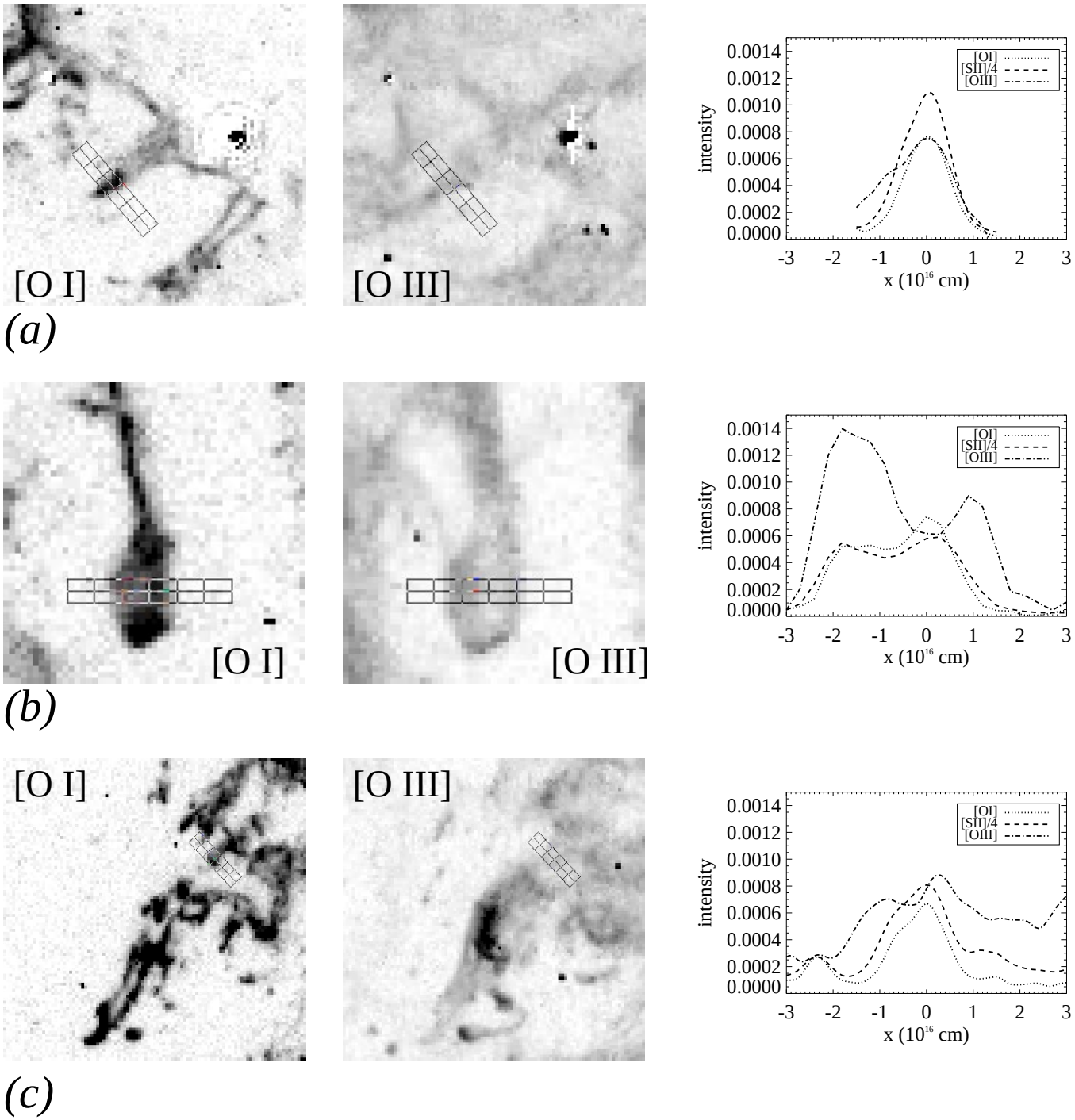

FIG. 6.—Three filaments, chosen to illustrate the different types of filamentary structures seen in the Crab: (*a*) filament D, (*b*) filament F, and (*c*) filament I. The [O I] and [O III] images are shown for each filament. Also shown are the reddening-corrected intensity profiles of [O I], [S II], and [O III] as a function of position across the filament. In each case the profiles are taken along the length and averaged across the width of the box shown in the images. All the plots use the same scale, and the "0" of the *x*-axis in each case corresponds to the center of the filament.

images (with FWHM = 0.″5) of each wide field (WF) frame were subtracted from the original frames, and pixels with values higher than a certain minimum in these difference frames were taken to represent regions of compact emission. The minimum pixel value determining the cutoff in each difference frame was chosen to be a fixed fraction of the average pixel value of bright compact features in the corresponding line filter image. We find that about 75%–80% of the [O I] emission arises in regions identified in this fashion, as compared with about 55%–60% of the [S II] emission and only about 10%–15% of the [O III] emission. The signal-to-noise ratio in the [O I] image and that in the [O III] image are about the same, and it is higher in the [S II] image. Therefore, although the numbers obtained above are somewhat uncertain because of difficulties in establishing a sky level in the images, it is clear that there is a significant difference between the degree of concentration of low-ionization emission and that of high-ionization emission.

The difference in the morphology of low-ionization gas and high-ionization gas is also seen in Figure 5. The top

TABLE 1

OBSERVED FILAMENT PROPERTIES

Parameter	Filament D	Filament F	Filament I
Width (10^{16} cm).....	~3	~6	>6
Peak $I_{[OI]}$.....	7.6	7.4	6.8
Peak $I_{[SII]}$	43.8	23.6	32.0
Peak $I_{[OIII]}$	7.5	9.0	8.9
$I_{[SII]}/I_{[OI]}$	6	4	7
$I_{[OIII]}/I_{[OI]}$	1	2	4

NOTE—The first row gives the total width of the filament as seen in the [O III] line. The peak intensities are given in units of 10^{-4} ergs s^{-1} cm^{-2} sr^{-1}.

panel is an He I λ5876 image and the bottom panel is an He II λ4686 image. The He I emission traces out individual filaments and knots and appears roughly comparable to the [S II] emission in its degree of concentration. Conversely, the only features visible in He II are extended parts of the "high-helium band" (e.g., Uomoto & MacAlpine 1987) in the WF2 field and the "hook" region (the "northern-hook" of Blair et al. 1997) in the WF4 field. While we do see these regions of diffuse emission, virtually no sharp structures are seen in the He II image, indicating that He II is more diffuse than even [O III], in which both diffuse and sharp structures are seen.

In addition to this general difference between diffuse high-ionization emission and compact low-ionization emission, many individual filaments also show a highly stratified ionization structure, while others do not. To illustrate the point we focus on the structure of three of the regions, D, F, and I, discussed by H96. (These are shown in Figs. 5–7 of that paper. Note that the labels for regions F and G need to be interchanged in Fig. 1 of H96.) These filaments lie toward the edge of the nebula and are therefore most likely to be lying in the plane of the sky. Such filaments have the lowest absolute radial velocities, and therefore Doppler shifting of line photons outside the bandpass of the filters is minimized. This in turn implies that errors in determining the intensities should be relatively low.

In Figure 6 we show the [O I] and [O III] images of the three filaments, together with [O I] λ6300, [S II] $\lambda\lambda$6731, 6716, and [O III] λ5007 intensity profiles across the filaments. Some properties of these three filaments are given in Table 1. The width of the filaments, determined by the extent of the [O III] emission, increases going from filament D to filament I. However, for all three filaments the [O I] profile has a central peak with an FWHM of about 0".3 (corresponding to about 10^{16} cm at the distance of the Crab). The peak [O I] intensity for all three filaments is $\sim 7 \times 10^{-4}$ ergs s^{-1} cm^{-2} sr^{-1}. The [S II] profile follows the [O I] in all three filaments; however, the peak intensity of the [S II] emission relative to the peak intensity of the [O I] emission is almost a factor of 2 higher for filament D than it is for filament F. In all three filaments, the peak intensity of the [O III] emission is about the same as the peak intensity of the [O I] emission. The total [O III]/[O I] ratio, however, increases as the [O III] zone becomes more extended.

The systematic variation in ionization structure is seen by comparing the [O III] profile with the [O I] profile. Filament D has a sharp-edged structure in which the emission from both [O I] and [O III] come from the same region. H96 suggest that filaments such as this result from R-T instabilities, in which the magnetic field is strong enough to suppress secondary Kelvin-Helmholtz instabilities during the growth of the filament, as well as strong enough to prevent the filament structure from responding much to thermal pressure. The filament can be thought of as being well confined by the strength of the field. Filament F is typical of "core-envelope" filaments, with an extended [O III] zone peaking about 10^{16} cm from the center, as defined by the peak of the [O I] emission. The filament is seen in the [O III] image as a bright envelope with a "hole" in the center. In filament I, the [O III] emission is from a relatively extended zone going out a few times 10^{16} cm from the center. In the picture of H96, filaments F and I are features in which formation of an envelope is less well suppressed by the magnetic field. The region containing filament I was cited as an example of an almost nonmagnetic R-T instability.

4. MODELING THE FILAMENTS

We used CLOUDY90 (Ferland 1997) to construct photoionization models of the three representative filaments described in the previous section. To account for the cylindrical symmetry of the filaments, we have weighted the emissivity from a given zone by its distance from the filament center while calculating the emergent flux. A similar procedure was followed by Péquignot & Dennefeld (1983) for their model M3a, where they weighted the outer zone of their one-dimensional model M3 higher than the inner zone to explain the high-ionization line strengths. In addition to these models, we calculated a constant density model to estimate the contribution of the more extended, high-ionization gas that is observed (see, e.g., Fig. 4).

The density structure, the incident flux, and the elemental abundances are the input parameters for the models. We used density profiles with a quadratic peak at the center and a surrounding exponential tail. This parameterization allows us to independently adjust the shape of the core and wings of the density profile to match the observed ionization structure. The incident continuum shape used for all models is the Crab continuum derived from DF and built into CLOUDY. The incident flux normalization was adjusted in conjunction with the density profiles to match the peak and shape of the [O I] λ6300 and the [O III] λ5007 intensity profiles. A single set of abundances was used for all models. The oxygen abundance was kept at the solar value relative to hydrogen, and the sulfur abundance was adjusted to match the peak intensity of [S II] relative to the peak intensity of [O I] in filament F. The resulting sulfur abundance was 0.7 times solar, corresponding to an S/O ratio of 0.015. The helium abundance was taken to be 2 times solar, corresponding to an He/H ratio of 0.2, in order to match the He I λ5876 to Hβ ratio of about 0.25 seen in the filaments. All other elemental abundances were kept at the solar value.

4.1. *Properties of Models D, F, and I*

The principal result of this paper is that by varying the input parameters as described above, we are able to obtain good matches to the observed properties of filaments D, F, and I. In Figure 7, the density profiles used for the three models (which we will refer to as models D, F, and I) are shown. Also shown are the normalized intensities of [O I] λ6300, [O II] λ3727, and [O III] λ5007 and the electron temperatures predicted by the models. These are the inten-

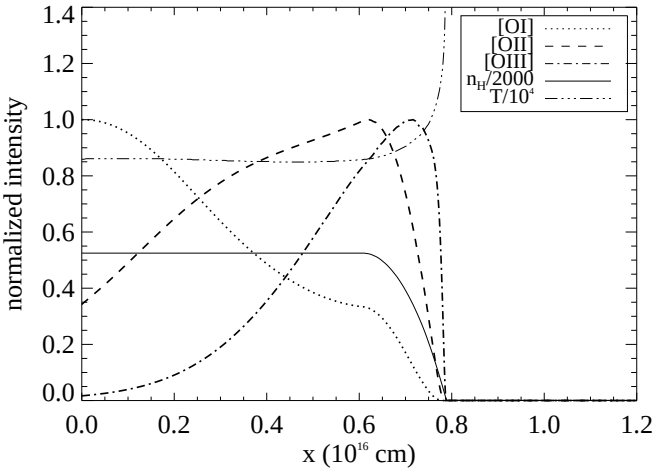

FIG. 7*a*

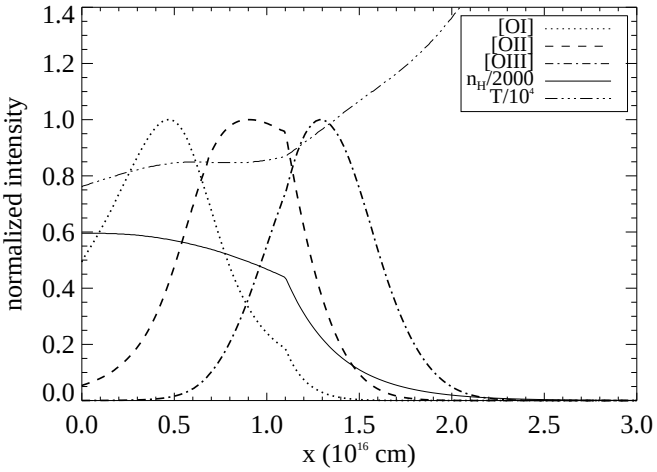

FIG. 7*b*

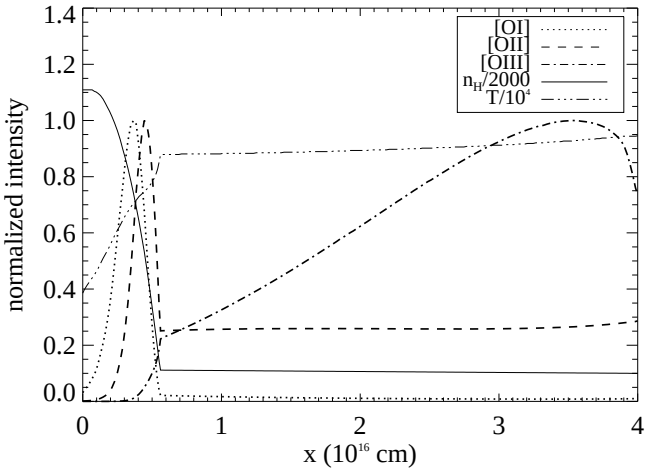

FIG. 7*c*

FIG. 7.—(*a*) Density structure used in Model D and predicted emissivities of [O I] λ6300, [O II] λ3727, and [O III] λ5007 and the electron temperature. (*b*) Same as (*a*) for Model F. (*c*) Same as (*a*) for Model I. These plots show the systematic change in the ionization structure of the models. The origin of the *x*-axis in each plot corresponds to the center of the filament.

sities and temperatures as predicted by the one-dimensional model and not weighted by radius. The input parameters of the models matching filaments D, F, and I are summarized in Table 2. The "core" and "envelope" hydrogen density columns (given in Table 2) serve as a convenient representation of the density profiles, which have a somewhat complicated parameterization as described in § 4 above.

In addition to these models, we ran a constant density model to investigate the characteristics of the general diffuse emission, such as the extended envelope surrounding filament I. We refer to this "constant envelope" model as model CE. Model CE uses a density $n_{\rm H} = 100$ cm^{-3}, an incident flux normalized to $10^{-16.3}$ ergs cm^{-2} s^{-1} at 1 ryd, and a thickness of 10^{17} cm. The abundances are the same as for the other three models. Since this model represents the diffuse gas surrounding the individual filaments, the assumed geometry is plane-parallel rather than cylindrical.

1. *The density and ionization structures*: Model D has a core extending out to about 0.8×10^{16} cm and an extremely low-density envelope from which there is essentially no emission. The [O I], [O II], and [O III] zones all lie within the core. The core for Model F goes out to about 1.1×10^{16} cm, beyond which the envelope falls off sharply. The [O III] zone lies mainly in the envelope, the [O II] zone lies across both core and envelope, while the [O I] zone is in

TABLE 2

INPUT PARAMETERS FOR MODELS

Parameter	Model D	Model F	Model I
Filament Radius (cm)	1.6×10^{16}	4.0×10^{16}	4.0×10^{16}
"Core" Hydrogen Column (cm^{-2})	7.7×10^{18}	1.2×10^{19}	9.1×10^{18}
"Envelope" Hydrogen Column (cm^{-2})	1.3×10^{16}	2.6×10^{18}	7.3×10^{18}
Central $n_{\rm H}$ (cm^{-3})	1050	1191	2218
log [F_ν(1 Ryd)]	−16.80	−16.80	−17.20

NOTE—The abundances for all models, in solar units, are as follows: He/H = 2.0 solar, S/H = 0.7 solar, and other abundances are solar.

the core. In the case of Model I, the core goes out to only 0.6×10^{16} cm, but it has an extended envelope of almost constant density. The [O III] zone lies in the envelope, and the [O I] and [O II] zones are in the outer part of the core. The column of hydrogen in the core and envelope of each model is given in Table 2.

2. *The central densities*: The peak hydrogen densities used are about 1000 cm^{-3} in Models D and F and about 2000 cm^{-3} in Model I. The central density used in model D is probably typical for filaments with such a structure and solar oxygen abundance, since a change in the central density would change the [O I] intensity. In the case of Models F and I, however, the [O I] emission falls off toward the center (Fig. 7). Therefore, in a filament similar to filament F or I, there could exist a region of very high density at the very center that is not traced by the [O I] emission and not resolvable in the WFPC2 images. A potential tracer of these regions is molecular hydrogen, which has been observed in the Crab filaments (Graham, Wright, & Longmore 1990) and which probably exists in regions of dense filaments interior to the neutral gas.

3. *The incident flux*: The shape of the incident continuum is fairly well established. The intensity of the incident flux, on the other hand, could vary from one filament to another. Models D and F have the incident flux normalized to $10^{-16.8}$ ergs cm^{-2} s^{-1} at 1 ryd, and Model I uses a flux normalized to $10^{-17.2}$ ergs cm^{-2} s^{-1} at 1 ryd. The flux at 1 ryd across a surface perpendicular to the incident radiation would be about 10^{-16} ergs cm^{-2} s^{-1} at the distance of the filaments from the center of the nebula. However, for the geometry R-T filaments we are considering, the filament face is oblique to the radiation, so that the ionizing flux is lower.

In order to compare these results directly with observations, we convolved the quasi–two-dimensional intensity profiles through the models with the resolution of the WF cameras. The results are shown in Figure 8, together with the observed [O I], [S II], and [O III] intensity profiles of Filaments D, F, and I. The observed profiles are the same as in Figure 6, except only half the filament, from the center out to the right edge, is shown in each case. The intensity axes are all plotted on the same scale so that all the observed and model profiles can be directly compared. In the case of model F, the predicted intensities have been multiplied by 0.5 to match the observed values. We believe that this is appropriate, in part because of the presence of dust extinction in the interiors of a number of these dense filaments (as discussed § 6).

The three models predict intensity profiles that match the data reasonably well. In particular, they match the observed intensities of [O I] λ6300, [S II] $\lambda\lambda$6716, 6731, and [O III] λ5007 while being consistent with the sizes of the filaments (Fig. 8). By constraining the models with only a limited set of line strengths, such as we have done here, a unique solution for the elemental abundances cannot be obtained (see, e.g., Davidson & Netzer 1979). However, it is perhaps worthwhile noting that our observations can be reproduced by models using elemental abundances that are close to solar.

The set of models D, F, and I, while constrained by observations of individual filaments are not simply meant to be models for particular filaments; rather, they are a representative of the individual filaments observed in the Crab. With the shape of the density profiles inferred from the observed morphology, and with common set of elemental abundances, these quasi–two-dimensional models reproduce the observed sequence of ionization structures.

4.2. *Model Spectra*

The systematic variation of morphologies of filaments leads to differences in the emitted spectra of filaments with distinct structures. In Table 3 we present the intensities of several lines relative to Hβ and the absolute Hβ line intensity for the four models. The line strengths for models D, F, and I are obtained by integrating the emissivity over the cylindrical symmetry. The absolute Hβ intensities presented

TABLE 3

MODEL PREDICTIONS OF LINE STRENGTHS

Line	λ	MD	MF	MI	CE
Hβ.....	4861	1.00	1.00	1.00	1.00
He I	5876	0.27	0.28	0.26	0.06
He II	4686	0.12	0.14	0.19	1.18
[C I]	9850	0.46	0.51	0.37	0.00
C III	1909	0.11	0.21	0.24	7.23
C IV	1549	0.00	0.02	0.00	5.11
[N I]	5200	0.08	0.14	0.08	0.00
[N II]	6584	3.69	3.74	3.57	0.31
[N II]	6548	1.25	1.27	1.21	0.10
[N II]	5755	0.04	0.04	0.04	0.01
[O I]	6300	0.39	0.60	0.30	0.00
[O I]	6363	0.12	0.19	0.10	0.00
[O II]	3727	7.98	8.29	9.97	1.24
[O III].....	5007	0.53	1.30	1.87	27.17
[O III].....	4959	0.18	0.45	0.65	9.41
[O III].....	4363	0.00	0.01	0.01	0.44
[S II]	6731	1.26	1.38	1.09	0.13
[S II]	6716	1.05	1.22	1.25	0.17
[S III]	9532	0.57	0.65	0.82	1.65
[Fe II].....	1.64 μm	1.89	2.20	1.67	0.00
$I_{H\beta}$.....	...	4.3×10^{-4}	3.9×10^{-4}	2.8×10^{-4}	1.3×10^{-4}

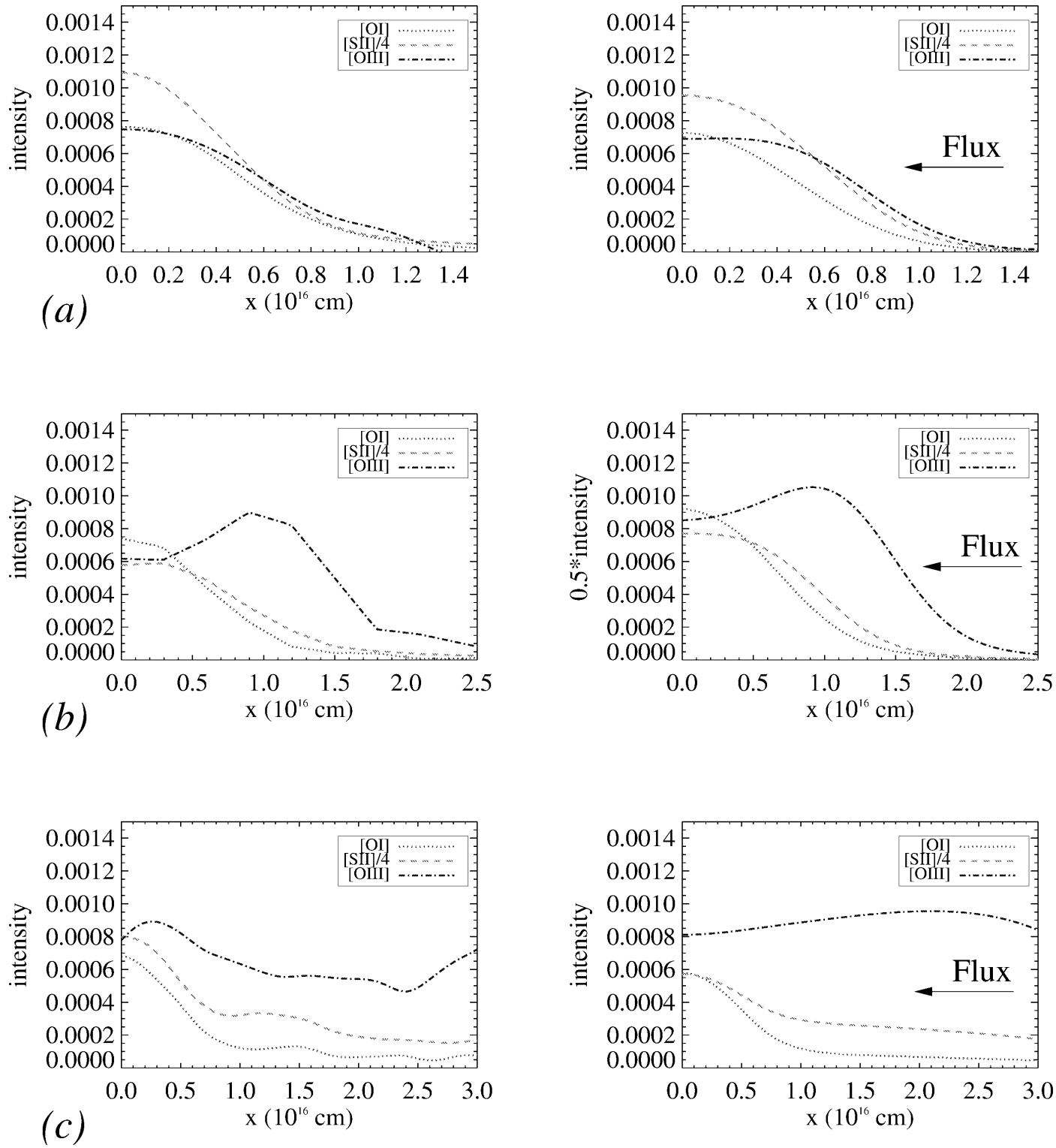

FIG. 8.—[O I], [S II], and [O III] profiles for observed (*left panels*) filament D (*a*), filament F (*b*), and filament I (*c*) compared with their respective model predictions (*right panels*). The observed profiles are the same as in Fig. 6 taken from the center to the right edge. To obtain the model profiles, the predicted one-dimensional profiles were integrated through a circular cross section, assuming that the filament was cylindrical, and then convolved to the resolution of the observations. The intensity scales are all the same to facilitate direct comparison. Note that for Model F, *half* the predicted intensity is plotted to correct for extinction by dust contained within the filament.

for these models are quoted per unit length of filament along the cylinder axis. The absolute Hβ intensity for model CE, however, is simply the emissivity integrated through plane-parallel structure.

The models reproduce the observed trend of an increasing prominence of high-ionization lines relative to low-ionization lines as the column through the envelope increases, going from Model D to I (Table 2) and further to model CE, which we may think of as a "pure envelope" model. The [O III] λ5007/[O I] λ6300 ratios for models D,

F, and I are 1.3, 2.2, and 6.3, respectively. The [S III] λ9532/[S II] λλ6716, 6731 ratio for the three models are 0.24, 0.25, and 0.35, respectively. The strength of low-ionization lines, such as [N I] λ5200, [O I] λ6300, and [Fe II] 1.64 μm, are highest in model F, which has the highest column in the core.

The envelope model CE is quite different from any of the models of filaments with dense cores. Model CE has very strong [O III] λ5007 emission and essentially no [O I] emission. The He I/Hβ ratio is also very different in model CE. He I λ5876/Hβ is nearly constant for the three filament models, which all use the same helium abundance. However, in the envelopes surrounding the filaments, the higher ionization state of He suppresses the He I emission. In model CE we find that for the same assumed abundance the He I/Hβ ratio is a factor of 5 lower than in the three filament models.

Model CE also predicts a relatively high ratio of C IV λ1549 to C III λ1909. Such a model could explain the *IUE* spectrum presented by Davidson et al. (1982) of a region including a bright filament (their Region 1), which shows strong C IV emission blueshifted by about 400 km s^{-1}. However, the high C IV emission seen symmetrically redshifted and blueshifted at 1100 km s^{-1} in a spectrum taken by the *Hopkins Ultraviolet Telescope* (Blair et al. 1992) cannot be explained by photoionization models and is actually the signature of a shock driven by the Crab synchrotron nebula into surrounding ejecta. This is discussed in detail by Sankrit & Hester (1997).

We have calculated the diagnostic [N II] and [O III] temperatures from the predicted spectra in the low-density limit (e.g., Osterbrock 1989), which is valid here because $n_H \ll 10^5$ cm^{-3} for all the models. The [N II] temperatures, calculated using the ratio $I(\lambda\lambda 6584 + 6548)$ to $I(\lambda 5755)$, for models D, F, I, and CE, are 8580 K, 8640 K, 8830 K, and 13,210 K, respectively; the [O III] temperatures, calculated using the ratio $I(\lambda\lambda 5007 + 4959)$ to $I(\lambda 4363)$, are 8980 K, 10,190 K, 9130 K, and 13,840 K, respectively. (Note: The temperatures were calculated using higher precision values; the numbers in Table 3 are given to two decimal places only.) These diagnostic temperatures represent emission-weighted averages of model temperatures within different ionization zones (Fig. 7).

The [N II] lines for filaments D, F, and I arise in the cores; therefore the range of [N II] temperatures is only ~250 K between filaments of different types. The [O III] lines, however, come from the envelopes, and so the range in [O III] temperatures is ~1200 K for this range of filament structures. The model CE is almost isothermal, and therefore both the [N II] and [O III] temperatures are ~14,000 K. However, the [N II] emission is much weaker in this model than in the other models, whereas the [O III] emission is much stronger (Table 3).

5. DISCUSSION

Many studies of ground-based spectra of Crab filaments have been published. In Table 4 we present a comparison between our observations and models and a few of these published spectra and previous photoionization models. We also present the [O III] and [N II] temperatures, calculated in the low-density limit as described in § 4.2. The rows are as follows: data from Table 1 of DF (the line strengths are representative of the entire nebula, obtained by amalgamating various sets of data; row 1); data for Miller (1978) position 2 (MIL2 in Table 4) considered by PD and model 3a of PD, which is their best-fit model for the position (rows 2 and 3); data for position 5 of Fesen & Kirshner (1982, hereafter FK) and HM's best-fit model to that spectrum (rows 4 and 5); similarly for position 8 of FK (rows 6 and 7); and filament D, model D, filament F, model F, filament I, model I, and model CE of this paper, with values for the models adapted from Table 3 (rows 8–14).

The observed ratio of He Iλ5876 to Hβ varies significantly for the different data sets. This ratio depends very strongly on the helium abundance (HM; Uomoto & MacAlpine 1987). Photoionization models can match the observations by using a suitable value for the helium abundance. The helium abundance (relative to hydrogen, by

TABLE 4

LINE STRENGTHS AND TEMPERATURES FROM A SELECTION OF OBSERVED SPECTRA AND MODELS

Model	[O I] λ6300 (1)	[O III] λ5007 (2)	[S II] λλ6716, 6731 (3)	$I_{HeI}/I_{H\beta}$ (4)	T([O III]) (5)	T([N II]) (6)
(1) DF [a]	9	100	60	0.46	16,060	...
(2) MIL2 [a]	6	100	29	0.89	12,140	8960
(3) PD3a [a]	5	100	19	0.69	12,370	8990
(4) FK5	12	100	67	0.17	<21,500	9,630
(5) HM5	16	100	55	0.16	16,000	...
(6) FK8	16	100	57	0.44	19,140	<12,130
(7) HM8	20	100	54	0.41	16,240	...
(8) D	100	100	600	0.2	...	...
(9) MD	74	100	592	0.27	8,980	8,580
(10) F	50	100	200	0.3	...	...
(11) MF	46	100	200	0.28	10,190	8,640
(12) I	25	100	175	0.3	...	...
(13) MI	16	100	125	0.26	9,130	8,830
(14) CE	0	100	1	0.06	13,840	13,210

NOTE.—DF, average observed values over the nebula; MIL2, FK5, FK8, observed positions; PD3a, HM5, HM8, corresponding best-fit models; D, F, I, MD, MF, MI, CE, observed filaments and models from this paper; see § 5 of text for details.

[a] The intensities in each of the two doublet lines of [O I] and [O III] are not separately reported. In these rows col. (1) is $I_{[OI]6300,6363}/I_{[OIII]4959,5007}$ and col. (3) is $1.33 \times I_{[SII]6716,6731}/I_{[OIII]4959,5007}$.

number) used by PD3a, HM5, and HM8 were 7 times solar, 1.5 times solar, and 4 times solar, respectively. For our models, we used a helium abundance of 2 times solar, as mentioned in § 4.

The most dramatic difference between our models and typical ground-based spectra is in the [O III] λ5007/[O I] λ6300 line ratio. The line ratio for the filaments we consider in this paper lies between ∼1 and ∼4 (Table 4). This is much lower than the ratio of ∼10 typical of ground-based spectra of the Crab (e.g., Miller 1978; Davidson 1978, 1979; FK; MacAlpine et al. 1989). The difference indicates that high-ionization emission in published spectra is generally dominated by the extended diffuse high-ionization component that fills the spectrograph aperture (also see Davidson 1987). Recall that we found that, above that, 90% of [O III] emission arises in this component, as compared with only 10% of the [O I]. Recall also that model CE showed strong high-ionization emission with very little low-ionization emission. Observed [O III] temperatures are also consistently higher than the ∼9000–10,000 K predicted by filament models. For example, FK obtain [O III] temperatures ranging from 11,000 to 19,000 K, Miller 1978 obtains 16,000 K and 12,000 K for two positions, and Davidson (1979) obtains a range of 12,000–17,000 K.

An additional complication is that some portion of the diffuse high-ionization emission that dominates many ground-based spectra of the Crab arises in a shock driven by the pressure of the synchrotron nebula (Sankrit & Hester 1997). The fact that many reported [O III] temperatures are well above that found even in "pure" envelope emission (e.g., model CE, unattenuated by any admixture of filaments) may point to a shock origin for a significant amount of observed high-ionization emission. Finally, we note that it is clear from examination of the *HST* images that ground-based spectra typically include emission from a number of physically discrete filaments.

The clear conclusion of this analysis is that ground-based spectra typically average over a very large range of physical conditions within the emitting region. This range of physical conditions is substantially greater than is accounted for by existing models, which generally assume constant density or constant thermal pressure within filaments. While the photoionization models of HM and PD are able to match the [O III] λ5007 and the [O I] λ6300 intensities simultaneously, the physical structure assumed in these models is not a good match to the structure seen in the *HST* images. This has potentially significant implications for results such as abundance determinations in filaments. For example, the models calculated by HM go out to about 2×10^{17} cm, with about two-thirds of it beyond the hydrogen ionization edge in order to account for the [O I] strength. Their values for the [S II] λλ6716, 6731 to [O I] λ6300 ratio are lower than what are observed and lower than what we obtain in our models, even though oxygen is depleted in their models while sulfur is not.

To us, it seems crucial that future efforts to interpret ground-based spectra of the Crab sort out the contributions from the various components lying within the aperture. While data such as those discussed in the present paper do not include enough lines to carry out a complete analysis of the spectra of individual filaments, we have shown that these data are quite adequate to constrain the density profiles and ionization structure of filaments. We conclude that future analyses of ground-based spectra should utilize ensembles of filament and diffuse models chosen to match the underlying physical structure seen in high spatial resolution images of the region containing the spectrograph aperture.

6. DUST IN THE FILAMENTS

Ground-based continuum images of the Crab have shown knots of extinction caused by the presence of dust in the nebula (Fesen & Blair 1990; Hester et al. 1990). These ground-based observations, at subarcsecond resolution, showed that the position of the dust knots coincided with bright filament cores. More recently, Hester et al. (1994) noted the presence of dust extinction in continuum images of the Crab Nebula obtained with the WFPC2. These dust features typically coincide with regions of low-ionization emission in the dense cores of filament heads. Similar features were also discussed by Blair et al. (1997) in the field that they observed with the WFPC2. They discuss specific features in their paper and point out that the amount of dust in the "rope" near position 1D of Fesen & Blair (1990) implies gas densities of about 40,000 atoms cm^{-3} if the gas-to-dust ratio has the normal interstellar medium (ISM) value. This large density is over 10 times higher than indicated by ionized gas line ratios. They also suggest that this implies a probable magnetic confinement for this feature.

Based on our analysis of the density profiles of filaments, we are able to approach the question of the dust-to-gas ratio in the Crab from a somewhat different direction. We selected a specific prominent dust feature to study. This is the filament from region G in Figure 6 of H96, and it corresponds to dust knot 4E of Fesen & Blair (1990). Figures 9*a–c* show the continuum image (centered on 5470 Å) and the [O I] and [O III] line images of the region. Profiles were extracted across the filament from these images and are plotted in Figure 9*d*. The continuum profile is inverted to bring out clearly its positional coincidence with the filament core. The plot shows that the dust closely follows the [O I]–emitting gas. The brightness across the dust feature in the continuum image is plotted in Figure 9*e*.

The extinction caused by dust in filament can be estimated from the reduction in the observed continuum intensity at the center of the filament. The unextincted continuum intensity is 24, and the continuum flux at maximum extinction is 16 (both values in the arbitrary units used in Fig. 9*e*). We also need to know what fraction of the continuum emission is coming from the synchrotron nebula in front of filament G (and is therefore unextincted by dust within the filament core). Since filament G is a long R-T filament lying toward the edge (e.g., Fig. 1) and growing more or less toward the center of the nebula, it is likely to be lying about midway into the synchrotron nebula. Therefore, we first assume that half the continuum intensity is from the foreground synchrotron nebula and the other half is extincted by the dust in the filament and estimate (Fig. 9*e*) that the extinction $A_{5470} = -2.5 \log (4/12) \sim 1.2$ mag at the filament center.

The details of the extinction at a given wavelength depend strongly on the grain properties and distribution of grain sizes. While such a detailed discussion is beyond the scope of this paper, we make some simplifying assumptions to obtain a rough estimate of the mass column of dust in the filament and the dust to gas ratio. Since we observe strong extinction at a wavelength in the visible, we assume a grain size of 7.5×10^{-6} cm, following Fesen & Blair (1990; see also Spitzer 1978, p. 158). At a wavelength of ∼5500 Å, the extinction efficiency (defined as the ratio of the actual

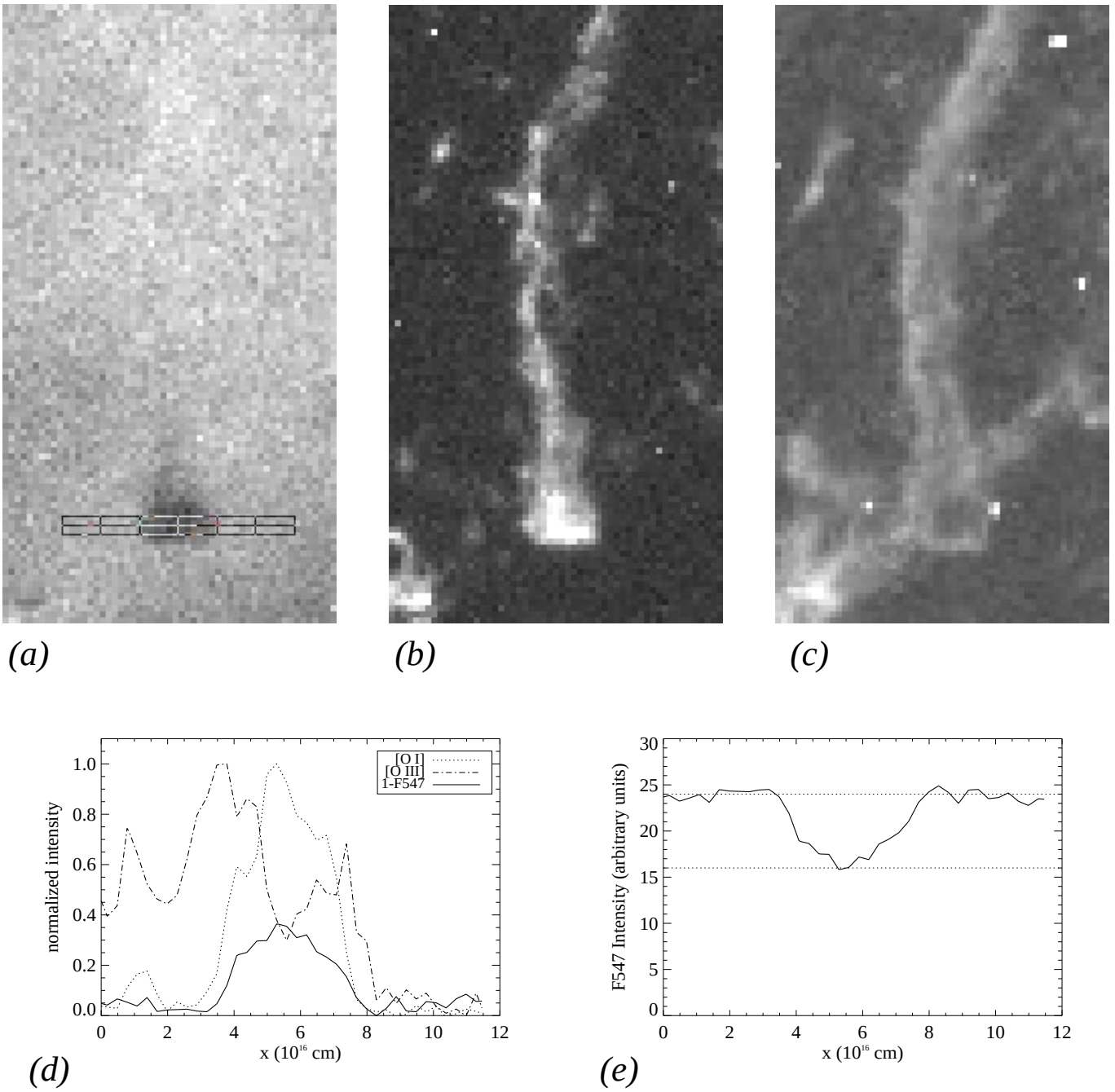

FIG. 9.—(*a*)–(*c*) Filament from region G, Fig. 6 of H96, as seen in the continuum F547M image, the [O I] image, and the [O III] image, respectively. The dark dust shadow is very well defined in the continuum image, and its position coincides with the bright [O I] core. (*d*) Profiles taken through the filament at the location shown by the box in (*a*). The [O I] and [O III] profiles are very similar to the profiles through filament F (Fig. 6). The dust profile is inverted to bring out clearly that its position is coincident with the [O I] peak. (*e*) Intensity (in arbitrary units) in the profile across the dust feature in the F547M image. The extinction seen is a lower limit, because some fraction of the continuum emission is from that part of the nebula lying in front of the filament.

extinction cross section to the geometric cross section of a grain) Q_e has a value of about 2 (Fig. 7.1 of Spitzer 1978). Adopting these values and using equation (7-1) of Spitzer (1978), we obtain a maximum dust column $N_{\rm dust} \sim 3 \times 10^{19}$ cm^{-2} through the center of the filament. Taking the bulk density of the dust to be 2 g cm^{-3} (Fesen & Blair 1990), this corresponds to a dust mass column, $M_{\rm dust} \sim 1.1 \times 10^{-5}$ g cm^{-2}.

In order to compare the mass of dust with the mass of gas in the filament, we make the further assumption that the density structure of filament G is reasonably well represented by our Model F, which is a model for a filament with similar structure (compare Fig. 9*d* with the filament F profiles in Fig. 6). The column of hydrogen for model F is $N_{\rm H} \sim 2.9 \times 10^{19}$ cm^{-2} through the filament center (Table 2; note that the value given in the table is for half the filament and needs to be multiplied by 2). For a helium abundance of 2 times solar, this corresponds to a gas mass column $M_{\rm gas} \sim 8.8 \times 10^{-5}$ g cm^{-2}. Thus the ratio of dust to gas in the filament, $M_{\rm dust}/M_{\rm gas} \sim 0.1$, which is an order of magnitude higher than the normal ISM value.

The result obtained above is assuming that filament G lies halfway into the synchrotron nebula. Filament G may actually be closer to the front of the nebula, in which case

the inferred extinction, A_{5470} would be lower. If we assume the extreme case, that filament G is lying in front of the synchrotron nebula, the extinction $A_{5470} = -2.5 \log (16/24) \sim 0.44$ mag (Fig. 9*e*). For a given set of grain properties, the dust mass column scales linearly with the extinction, and so in this case $M_{\rm dust} \sim 4.0 \times 10^{-6}$ g cm^{-2}. The ratio of dust to gas is therefore $M_{\rm dust}/M_{\rm gas} \sim 0.05$, which is still about five times higher than the normal ISM value.

The strong extinction by dust in the filament cores indicates a high dust content and a high dust-to-gas mass ratio. However, it is necessary to make the caveat that a number of assumptions about grain properties have gone into our calculation. The size distribution and optical properties of grains in the Crab filaments are not known. However, larger grains would tend to increase the mass column of dust, since the extinction efficiency increases at most by a factor of $\lesssim 2$ (Spitzer 1978), while the mass of a grain goes as the cube of its radius. It is unlikely that grains that are very much smaller can extinguish 5500 Å emission efficiently.

There may be a very high-density region at the filament center, which is not traced by the [O I] and not resolved in the WFPC2 images. While this is possible (see discussion in § 4.1), the dust follows the [O I] emission and is definitely not confined to this extremely narrow ($<0\farcs1$) region. If the overall dust-to-gas ratio is to be close to the ISM value, it would require not only high central densities but also a decoupling of the dust from the gas, since this ratio in the [O I]–emitting region is higher than the ISM value.

The question of dust in the Crab filaments deserves further, more detailed study. A high dust content implies that much of the heavy elements produced by the supernova and the progenitor star are depleted from the gas phase and locked up in solids. Accurate values for the dust content of filaments and knowledge of the grain compositions are crucial for understanding the elemental abundances in the Crab. The filament cores where dust is seen are also likely to be the sites where molecular hydrogen forms. Molecular hydrogen has been observed in the Crab filaments by Graham et. al (1990) in the prominent bright structure seen, for example, in the upper left quadrant of Figure 3. Both Fesen & Blair (1990) and Blair et al. (1997) have pointed out the existence of dust features in this region. Mapping the H_2 emission would be important for understanding the interaction between the gas and the dust in the Crab Filaments.

7. SUMMARY

We have presented high spatial resolution narrowband images of filaments in the Crab Nebula in a range of emission lines. These images show very obvious differences in the structure of high- and low-ionization emission in the Crab. The emission from low-ionization potential species is concentrated in compact regions: knots and filaments with transverse dimensions that are typically well under an arcsecond. Conversely, emission from high-ionization potential species comes predominately from more extended regions. We also find that individual filaments lie along a sequence from sharp-edged narrow filaments with no observable ionization stratification to filaments with low-ionization cores and extended high-ionization envelopes. This sequence is discussed by H96, who attribute it to the nonlinear development of magnetic R-T instabilities in the Crab.

We present cylindrically symmetrical photoionization models of filaments that are representative of this sequence. In particular, these models match the observed [O I] λ6300 to [O III] λ5007 and [S II] $\lambda\lambda$6716, 6731 to [O III] λ5007 line ratios of the filaments while being consistent with the filament sizes. The success of these models demonstrates that the broad range of observed ionization structures can be explained as photoionization of the density structures resulting from R-T instabilities. Viewed another way, our results show that dramatic differences in the ionization structure and the integrated spectrum of filaments can result from the dynamical processes responsible for filament formation. We also find that, because of the small scales of the structures within the Crab, ground-based spectra invariably integrate over a number of physically discrete structures with a range of characteristics. This difficulty with interpretation of existing ground-based spectra is seen especially well in the difference between the [O III]/[O I] ratio in our models and data and the [O III]/[O I] ratio in previous observations and models. It is also worth noting that while the He I/Hβ ratio is nearly constant for all filament models, it is much lower in the extended high-ionization "envelope" emission. We conclude from this analysis that reliable interpretation of spectra of Crab filaments requires specific information about the physical structure of filaments obtained from high spatial resolution images in a few lines.

Finally, we find that dust extinction in Crab filaments can complicate interpretation of filament spectra. In one feature we find that the observed extinction may require a dust-to-gas mass ratio that is an order of magnitude higher than normal ISM values.

We thank the referee for a number of useful suggestions that improved the presentation of the ideas in this paper. This work was supported by NASA contract NAS 7-1260 to the WFPC2 IDT. This work was supported at ASU by NASA/JPL contracts 959289 and 959329.

REFERENCES

Blair, W. P., et al. 1992, ApJ, 399, 611
———. 1997, ApJS, 109, 473
Chevalier, R. A., & Gull, T. R. 1975, ApJ, 200, 399
Davidson, K. 1978, ApJ, 220, 177
———. 1979, ApJ, 228, 179
———. 1987, AJ, 94, 964
Davidson, K., & Fesen, R. A. 1985, AR&A, 23, 119
Davidson, K., & Netzer, H. 1979, Rev. Mod. Phys., 51, 715
Davidson, K., et al. 1982, ApJ, 253, 696
Ferland, G. J. 1997, Univ. Kentucky Dept. Phys. Astron. Internal Rep.
Fesen, R. A., & Blair, W. P. 1990, ApJ, 351, L45
Fesen, R. A., & Kirshner, R. P. 1982, ApJ, 258, 1
Graham, J. R., Wright, G. S., & Longmore, A. J. 1990, ApJ, 352, 172
Henry, R. B. C., & MacAlpine, G. M. 1982, ApJ, 258, 11
Hester, J. J., et al. 1990, ApJ, 357, 539
Hester, J. J., et al. 1994, BAAS, 26, 951
———. 1996, ApJ, 456, 225
Holtzman, J. A., et al. 1995, PASP, 107, 1065
Jun, B-I. 1998, ApJ, 499, 282
Jun, B-I., Norman, M. L., & Stone, J. M. 1995, ApJ, 453, 332
MacAlpine, G. M., et al. 1989, ApJ, 342, 364
Miller, J. S. 1978, ApJ, 220, 490
Osterbrock, D. E. 1989, in Astrophysics of Gaseous Nebulae and Active Galactic Nuclei (Mill Valley: Univ. Sci. Books), 121
Péquignot, D., & Dennefeld, M. 1983, A&A, 120, 249
Sankrit, R., & Hester, J. J. 1997, ApJ, 491, 796
Spitzer, L. 1978, Physical Processes in the Interstellar Medium (New York: Wiley)
Uomoto, A., & MacAlpine, G. M. 1987, AJ, 93, 1511